Closed-loop control of targeted ultrasound drug delivery across the blood–brain/tumor barriers in a rat glioma model

Tao Sun[a,b,1], Yongzhi Zhang[a], Chanikarn Power[a], Phillip M. Alexander[a], Jonathan T. Sutton[a], Muna Aryal[a], Natalia Vykhodtseva[a], Eric L. Miller[b], and Nathan J. McDannold[a]

[a]Focused Ultrasound Laboratory, Department of Radiology, Brigham and Women's Hospital, Harvard Medical School, Boston, MA 02115; and [b]Department of Electrical and Computer Engineering, Tufts University, Medford, MA 02155

Edited by Robert Langer, Massachusetts Institute of Technology, Cambridge, MA, and approved October 16, 2017 (received for review July 27, 2017)

Cavitation-facilitated microbubble-mediated focused ultrasound therapy is a promising method of drug delivery across the blood–brain barrier (BBB) for treating many neurological disorders. Unlike ultrasound thermal therapies, during which magnetic resonance thermometry can serve as a reliable treatment control modality, real-time control of modulated BBB disruption with undetectable vascular damage remains a challenge. Here a closed-loop cavitation controlling paradigm that sustains stable cavitation while suppressing inertial cavitation behavior was designed and validated using a dual-transducer system operating at the clinically relevant ultrasound frequency of 274.3 kHz. Tests in the normal brain and in the F98 glioma model in vivo demonstrated that this controller enables reliable and damage-free delivery of a predetermined amount of the chemotherapeutic drug (liposomal doxorubicin) into the brain. The maximum concentration level of delivered doxorubicin exceeded levels previously shown (using uncontrolled sonication) to induce tumor regression and improve survival in rat glioma. These results confirmed the ability of the controller to modulate the drug delivery dosage within a therapeutically effective range, while improving safety control. It can be readily implemented clinically and potentially applied to other cavitation-enhanced ultrasound therapies.

drug delivery | focused ultrasound | acoustic cavitation | treatment control | blood–brain barrier

Focused ultrasound (FUS) is a noninvasive therapeutic technology that directs acoustic energy to deep tissue targets without incisions or radiation. Currently, most clinically adopted FUS treatment methods harness thermal effects resulting from the convergence of high-pressure ultrasound beams at the focus to ablate tissue (1), a process that can be monitored and controlled by magnetic resonance (MR) thermometry (2, 3) or standard B-mode ultrasonic imaging (4). Another family of FUS therapies utilize biologically inert and preadministrated microbubbles, which reradiate low-intensity, incident ultrasound to further localize and amplify the mechanical effects onto the vasculature. The targeted mechanical effects can result in various beneficial biological effects, including the cellular and/or transcellular permeability enhancement [blood–brain barrier disruption (BBBD) (5–7) and sonoporation (8)], thrombolysis (9), or nonthermal ablation (10). BBBD, the subject of the current study, reversibly opens the blood–brain barrier (BBB) enabling the delivery of even large-molecule therapeutics to the central nervous system and offers great potential for treating multiple neurological disorders. This technology has been demonstrated in rodent (11–16) and nonhuman primate (17, 18) models, and clinical trials are underway (19, 20).

There exists an unmet need for reliable treatment monitoring and control of this technique to ensure that a safe and effective acoustic exposure level is maintained. Contrast-enhanced magnetic resonance imaging (MRI) has been employed for BBBD detection and damage evaluation (5, 17–19, 21). Although it is effective, the imaging occurs after sonication and is relatively time-consuming. Further, vascular damage may take tens of seconds to manifest itself in MRI, limiting the technique's utility as a control tool. MRI is also expensive and technically challenging, which could limit widespread clinical use.

Control may also be realized through indirect means by measuring acoustic signals or other physical markers. Unlike thermal therapies, for which MR thermometry enables temperature control, the sonications used for FUS-induced BBBD do not produce significant temperature changes. Instead, the sonications utilize the mechanical effects of bubble oscillations on the brain vasculature. This microbubble activity, known as acoustic cavitation, ranges from sustained, low-amplitude bubble oscillations (stable cavitation), to transient bubble collapse (inertial cavitation) (22, 23). Monitoring and control of cavitation behaviors using passive cavitation detection (PCD) may be a feasible approach for treatment control. PCD relies on the distinct Fourier spectra of microbubble emission signals, in which the strength of stable cavitation hallmarks (harmonics, subharmonics, and ultraharmonics) and inertial cavitation markers (broadband response) can be quantified in real time. These cavitation metrics characterize the acoustic signatures of microbubble

Significance

Focused ultrasound is currently the only method of reversible blood–brain barrier disruption for targeted drug delivery without incision or radiation. A significant challenge for its clinical translation is a lack of reliable real-time treatment control. Here a closed-loop, real-time control paradigm is shown capable of sustaining stable microbubble oscillations at a preset level while minimizing microbubble behavior that may result in vascular damage. Tested at clinically relevant frequency in healthy and tumor-bearing rats, our approach enables targeted delivery of predefined drug concentrations within a therapeutically effective range in both normal tissue and glioma, while maintaining a safe exposure level. It can be readily implemented clinically for delivering chemotherapeutics or other agents and potentially applied to other cavitation-enhanced ultrasound therapies.

Author contributions: T.S. and N.J.M. designed research; T.S., Y.Z., C.P., P.M.A., J.T.S., and M.A. performed research; T.S. and N.V. analyzed data; and T.S., J.T.S., N.V., E.L.M., and N.J.M. wrote the paper.

Conflict of interest statement: Two provisional patents describing the controlling system and focused ultrasound system developed in this work have been filed (inventors: N.J.M. and T.S.). N.J.M. holds another two published patents on the ultrasound technique evaluated in this work. No conflicts of interest were disclosed by the other authors.

This article is a PNAS Direct Submission.

[1]To whom correspondence should be addressed. Email: taosun@bwh.harvard.edu.

This article contains supporting information online at www.pnas.org/lookup/suppl/doi:10.1073/pnas.1713328114/-/DCSupplemental.

oscillations and have been correlated with many cavitation-induced bioeffects, including BBBD. In general, it has been well-accepted that the successful BBBD can be facilitated once the strength of stable cavitation achieves a certain threshold. However, if the exposure level is too high, the likelihood of inertial cavitation increases, which has been reported to be associated with vascular/neuronal damage (7).

Despite various investigations of PCD monitoring during FUS-induced BBBD, a closed-loop cavitation controller that can modulate BBBD and prospectively predict drug concentrations in the brain while simultaneously avoiding damage from inertial cavitation is still lacking. McDannold et al. (24) proposed the potential of using microbubble emissions to control the BBBD, based on a correlation found between the strength of second/third harmonic components and MRI contrast enhancement post BBBD. This potential has been further suggested by several BBBD works with cavitation monitoring (21, 25–27) and other microbubble-mediated therapies (28, 29). O'Reilly and Hynynen (30) designed an active controller that increases the acoustic pressure until ultraharmonic emission is detected and then reduces it by a predetermined amount. The pressure levels were found to be associated with MRI contrast enhancement and damage occurrence. However, this controller becomes open-loop after ultraharmonics are detected, leaving the rest of the sonication uncontrolled. Moreover, its performance relies on the detection of ultraharmonics, which may be challenging in the presence of the skull (25), in the varying ambient pressure (31), or in the case of a high broadband noise level. Having a method to further control the exposure level would be desirable and could enhance confidence that an appropriate exposure level is maintained. In the present work, we investigated the use of harmonic emission (HE) and broadband emission (BE) to characterize the strength of stable and inertial cavitation, respectively.

Additional challenges for establishing a reliable yet clinically translatable cavitation controller arise due to the varying microbubble concentration over time after injection and the possible heterogeneous spatial distribution of cavitation seeds. First, owing to the destruction of microbubbles under FUS exposure and the physiological dissolution kinetics of bubbles in circulation, the amount of cavitation seeds will decrease during the sonication. Left unchecked, a reduction in the microbubble concentration in the targeted area can result in a controller choosing exposure levels exceeding safe conditions. Second, for brain cancer treatments, the vascular density in the tumor is heterogeneous, and other factors such as vessel size, blood flow, and the response of the partially intact blood–tumor barrier (BTB) could differ from the normal brain. The spatial microbubble distributions may thus vary for tumor-bearing targets, challenging the robustness of controlling performance.

In addition, microbubble dynamics are affected by several key acoustic parameters. Apart from acoustic pressure and frequency, the pulse repetition frequency (PRF) of the transmitted ultrasound might affect the microbubble behavior in the confined environment of the brain microvasculature. For example, theory and experiments indicate that radiation forces, which may be involved in the BBBD, can depend on the PRF (32). Further, a recent study (33) using long therapeutic exposure (5-ms bursts at 1 MHz) observed bubble aggregation at the later stage of sonication, which signaled the dominance of secondary over primary radiation force. Moreover, using a higher PRF transmits the same ultrasound energy in a shorter time, maximizing the exposure when there exist more cavitation seeds in the circulation.

Here we developed and validated a fully closed-loop cavitation emission-based controlling paradigm for modulating drug delivery via BBBD. By sustaining stable cavitation while suppressing inertial cavitation, our objective was to deliver a prescribed drug dose and keep the brain damage-free. The present work was accomplished by the following steps. First, we designed a dual-aperture FUS system to achieve targeting specificity at a clinically relevant FUS frequency. The feasibility of controlling the cavitation behavior was confirmed by measuring HE–pressure linearity and the BE thresholds. Next, we optimized the acoustic performance of the controller during BBBD in vivo with different PRF values and microbubble administration protocols. Using optimal settings, we investigated the association between HE strength and the delivery of a model drug [Trypan Blue (TB)]. Based on this calibration, we tested if we could deliver a predetermined amount of drug by sonicating until the integrated HE reached a preset goal. Finally, we investigated the controlled delivery of a larger and clinically used agent, liposomal doxorubicin (DOX), in the F98 rat glioma model.

Results

Cavitation Monitoring Calibration Using a Dual-Aperture FUS System.

A dual-aperture FUS setup ($f_{\mathrm{central}} = 274.3$ kHz) with a passive cavitation detector ($f_{\mathrm{central}} = 650$ kHz) was designed and built in house (Fig. 1*B*). It served as the core hardware of inducing and sensing cavitation effects while drug delivery was facilitated (Fig. 1*A*). The combined focus of the two transducers significantly improved beam focusing in the axial direction due to the enlarged effective aperture size (34). However, two coherent wave sources will yield an interference pattern, which would result in inhomogeneous BBBD. To redistribute the acoustic energy at focus and produce spatially homogenous BBBD, we drove each aperture with a slight offset ($\Delta f = 31$ Hz), modulating the interference pattern over the course of each burst. This design enabled a fully constrained and homogenous treatment profile in the rat brain at a clinically relevant frequency range. Detailed design and acoustic performance demonstration were published elsewhere (35).

A pilot study was performed to characterize the HE and BE recordings at different pressure amplitudes and microbubble doses. We sonicated targets in striatum and hippocampus in both hemispheres using a positive ramping pulse train without feedback control until BE was detected. Plots of HE in dB as a function of acoustic pressure were highly linear, and this linearity was improved as the microbubble dose was augmented (Fig. 2 *A* and *B*). A 200 μL/kg microbubble dose offered the most linear HE–pressure response for both striatum ($R^2 = 0.94 \pm 0.03$) and hippocampus ($R^2 = 0.95 \pm 0.02$) targets. Optison doses of 50 μL/kg produced the least linear response ($R^2 = 0.28 \pm 0.20$ for striatum and $R^2 = 0.35 \pm 0.22$ for hippocampus), whereas 100 μL/kg resulted in $R^2 = 0.60 \pm 0.22$ for striatum and $R^2 = 0.70 \pm 0.15$ for hippocampus. The less-robust linearity observed with lower microbubble doses reflects the weaker acoustic emission signals (near the noise floor) produced by a smaller number of cavitation sources. ANOVA showed statistical significance for both factors—microbubble dose ($P < 0.0001$) and targeted location ($P = 0.035$)—although multicomparison tests suggested no significant differences between two the targets for all three Optison doses.

The maximum HE level achieved without detectable BE was found to be positively correlated with microbubble dose (Fig. 2*C*). ANOVA demonstrated statistical significance for the factor of microbubble dose ($P < 0.0001$) but not targeted location ($P = 0.732$). Correspondingly, the lowest pressure level where BE was detected decreased at higher doses (Fig. 2*D*). Although multicomparison tests suggested no significant differences between two targets for all three Optison doses, ANOVA suggested targeted location was a significant factor ($P = 0.033$), as well as microbubble dose ($P < 0.0001$). In summary, a microbubble dose of 200 μL/kg produced the most linear HE–pressure response and the largest controlling window (the maximum HE level

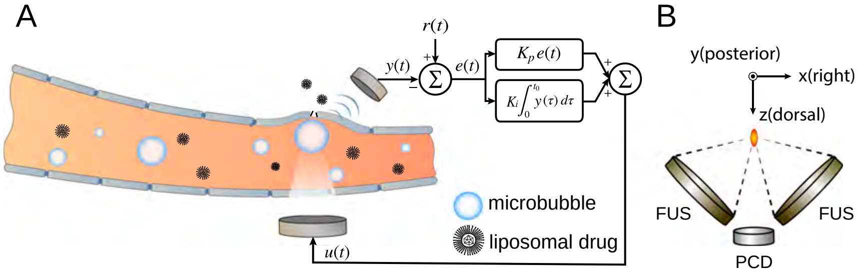

Fig. 1. The controller system. (*A*) Schematic representation of the feedback controlled drug delivery system. Serving as the acoustic indicator of drug delivery dosage, microbubble emission signal *y*(*t*) was recorded and compared with the expected value *r*(*t*). Their difference *e*(*t*) was used to calculate the controller output *u*(*t*), which was fed back to the focused ultrasound transducer for controlling the transmission. (*B*) Illustration of the dual-aperture focused ultrasound setup with a passive cavitation recording transducer.

without BE detection). Therefore, this dose was used in all of the following studies for testing the controller performance.

Optimizing the Controller Performance. To optimize the controller performance, we next performed a study investigating the stability of the HE signals under feedback control for two different pulse repetition frequencies and two microbubble infusion protocols. Our feedback controller was designed as an adaptive proportional–integral controller (Fig. 1*A*). The proportional gain K_p was set initially based on the data shown in Fig. 2*A*. Once HE reached the desired range, it was decreased by 70% to minimize overshoot. The HE range used for the desired goal was that found in Fig. 2 to be slightly below the maximum HE level achieved without BE detection. The integration term of the controller (total HE) was monitored and used as a set point to terminate the sonication. Because only minor differences in HE between striatum and hippocampus were observed (Fig. 2 *B* and *C*), in subsequent experiments we combined the results from the two targets. All controller settings were kept the same except for the maximum pressure limits, which were set based on the BE thresholds assessed in Fig. 2*D* (two SDs below the mean BE threshold: 0.66 and 0.54 MPa for striatum and hippocampus targets, respectively). Results of this study are shown in Fig. 3.

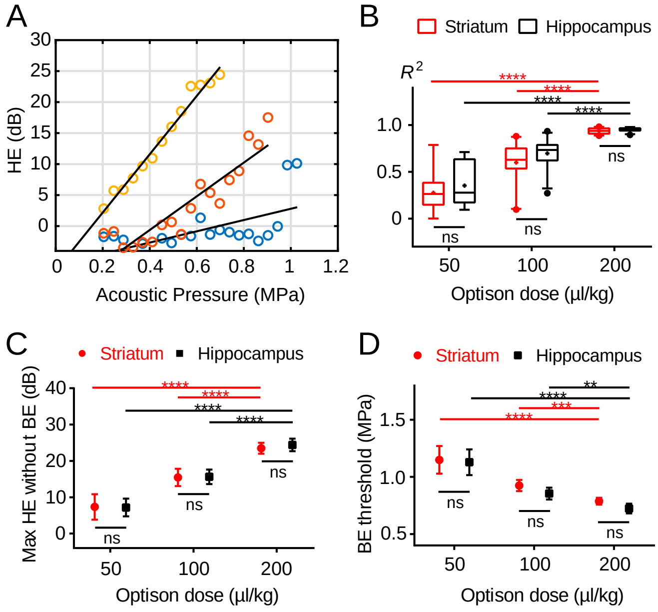

Fig. 2. Open-loop feasibility test in vivo. (*A*) Representative examples showing HE recorded during sonication in the striatum as a function of acoustic pressure with a 50 (in blue), 100 (in red), or 200 (in orange) µL/kg bolus microbubble administration. Black lines were shown as the corresponding linear regressions. (*B*) Coefficient of determination R^2 of the linear correlations between HE and acoustic pressure for the three bubble doses. The most linear relationship occurred with 200 µL/kg microbubble administrations for both striatum ($R^2 = 0.94 \pm 0.03$) and hippocampus ($R^2 = 0.95 \pm 0.02$) targets. (Box limits, 25 and 75 percentiles; whiskers, 5 and 95 percentiles; center line, median; +, mean.) (*C*) Maximum HE reached before BE was detected. (*D*) BE thresholds, i.e., lowest pressures at which BE was detected. Error bars represent 95% confidence intervals. Two-way ANOVA with post hoc multicomparisons was used to assess significant difference. (**$P < 0.01$; ***$P < 0.001$; ****$P < 0.0001$.)

With a bolus injection (Fig. 3 *A*–*C*), the microbubble concentration was not constant. Sonications with PRFs of 1 and 4 Hz were compared with the same number of pulses. Since the pulses were delivered over a shorter time with a 4-Hz PRF, the stability of the HE over the course of the sonication was improved compared with 1 Hz (Fig. 3*A*), and the number of pulses in the desired HE range was higher (Fig. 3*B*). Furthermore, the acoustic input increased more smoothly with a 4-Hz PRF, and the controller did not reach the preset maximum exposure level until the end of the sonication (Fig. 3*C*). In contrast, with 1 Hz the HE decreased over time as the microbubble concentration diminished.

Although stable HE was achieved with a 4-Hz PRF, the controller profile was not optimal because of this microbubble loss during sonication, which led to a continual increase in the FUS exposure level. We therefore investigated whether a slow microbubble infusion administered after the initial bolus could improve the controller performance (Fig. 3 *D*–*F*). The use of this infusion improved the stability of the HE for the 1-Hz PRF sonications and reduced the rate of increase in pressure amplitude for the 4-Hz PRF sonications. Statistical comparisons for all of the 1- and 4-Hz PRF sonications for both bolus and infusion administration are shown in Fig. 3 *G* and *H*. The good burst rate (GBR) measured the percentage of pulses where HE was in the desired range. ANOVA indicated statistical significance for both factors, PRF ($P = 0.001$) and bubble administration mode ($P = 0.001$). Multicomparison post hoc tests suggested that a 4-Hz PRF and infusion injection significantly improved the GBR compared with both bolus injection groups. Sonication with a 4-Hz PRF using infusion injection was also superior in sustaining HE within the desired range. Using an infusion also reduced the likelihood for BE (33.7% and 16.7%, respectively, for bolus and infusion; 4-Hz PRF) because the microbubble concentration was sustained and the exposure level did not need to be increased as much.

Controlled Delivery of a Model Drug to the Brain. Using the optimal settings (4-Hz PRF and microbubble infusion administration) found above, we next investigated whether the integrated HE signal is correlated with the amount of a tracer (TB) delivered to

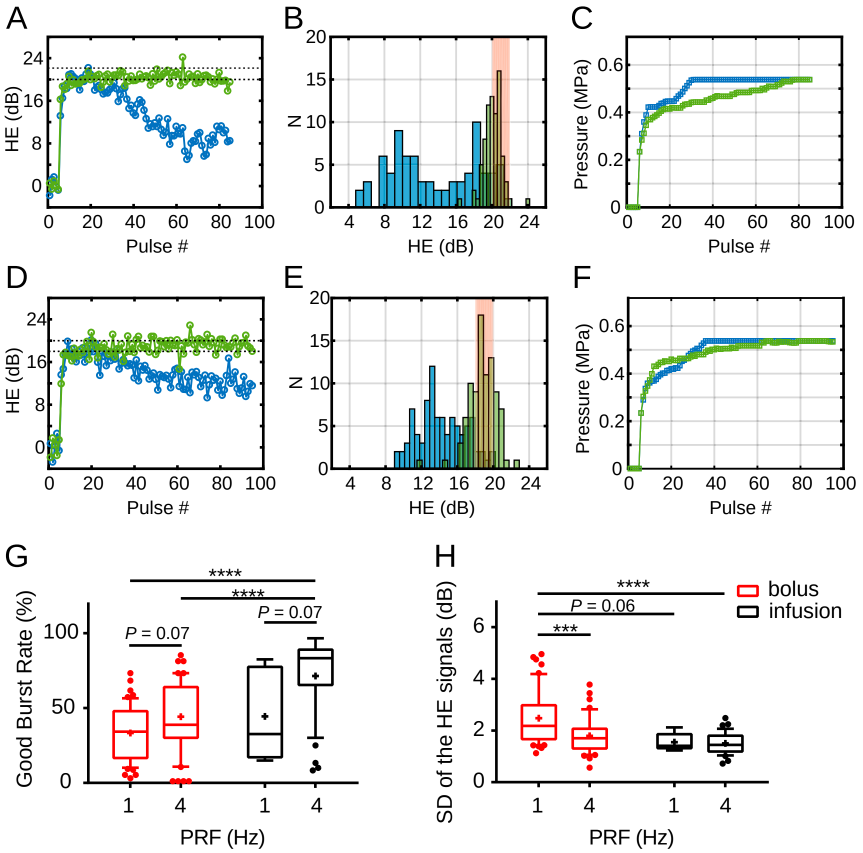

Fig. 3. Optimizing the acoustic performance of the closed-loop controller. (*A*) Representative HE profiles for two sonications of the same target with 1-Hz (in blue) versus 4-Hz (in green) PRF. The desired HE range was shown as black dashed lines. (*B*) Histograms of the two HE profiles shown in *A*. (*C*) Sonication input (acoustic pressure) profiles for the two examples shown in *A*. (*D*) Representative HE profiles for two sonications of the same target using 4-Hz PRF with bolus (in blue) versus infusion (in green) administration of Optison microbubbles. (*E*) Histograms of the two HE profiles shown in *D*. (*F*) Sonication input profiles for the two examples shown in *D*. (*G* and *H*) Statistical comparisons for all of the 1- and 4-Hz PRF sonications for both bolus and infusion administrations (1 Hz + bolus, $n = 55$; 4 Hz + bolus, $n = 53$; 1 Hz + infusion, $n = 6$; 4 Hz + infusion, $n = 36$). (*G*) Statistical comparison of the good burst rate (GBR), which measured the percentage of pulses where HE was in the desired range. ANOVA showed statistical significance for both factors, PRF ($P = 0.001$) and microbubble administration mode ($P = 0.001$). Multicomparison tests suggested 4-Hz PRF using infusion injection significantly improved the GBR compared with the bolus injection groups. (*H*) HE stability comparison assessed by the SD of the HE signals. ANOVA showed significance for PRF ($P = 0.003$) but not bubble administration mode ($P = 0.07$). Multicomparison tests suggested that 4 Hz with microbubble infusion was superior in sustaining HE stability to 1 Hz with bolus injection. (Box limits, 25 and 75 percentiles; whiskers, 5 and 95 percentiles; center line, median; +, mean. Statistical significance was assessed via two-way ANOVA with a Tukey multicomparison test; ***$P < 0.001$; ****$P < 0.0001$.)

the brain (Fig. 4*A*). Our assumptions here were that the magnitude of the BBBD (and the amount of the tracer delivered) is reflected by the strength of the stable cavitation and that the effects are additive as more bursts are applied. If these assumptions are correct, then the total stable cavitation enhancement ($\mathrm{HE}_{\mathrm{total}}$) can serve as an acoustic marker for the cumulative mechanical/biological effects. To test this, sonications were performed in 21 locations in the striatum and hippocampus with different sonication durations (60, 90, and 120 s; $n = 7$ for each duration). The duration was varied to produce a range of both $\mathrm{HE}_{\mathrm{total}}$ and BBBD magnitude. The relationship between $\mathrm{HE}_{\mathrm{total}}$ and TB fluorescence enhancement for these sonications is shown in Fig. 4*B*. This data were fit using segmented linear regression to model a threshold for BBBD, and a good overall correlation was observed ($R^2 = 0.80$; Fig. 4*B*). We found four cases (labeled as non-BBBD cases in Fig. 4*B*) in which the fluorescence intensity was less than two SDs above the mean value found in control animals that did not receive FUS ($n = 10$ for each sonication target).

Based on the calibration curve shown in Fig. 4*B*, we next investigated if we could deliver a desired amount of TB by sonicating until the integrated HE reached a preset goal. The resulting fluorescent intensity enhancement (green symbols in Fig. 3*B*) agreed within error estimates with the reference curve for three different goals: 1,500 dB ($n = 4$), 2,100 dB ($n = 8$), and 2,700 dB ($n = 5$), suggesting that this controller enabled us to deliver a predetermined amount of TB to the brain.

To verify the successful suppression of histological damage, hematoxylin and eosin (H&E) stained sections were examined for the animal with the highest $\mathrm{HE}_{\mathrm{total}}$ (shown in Fig. 4*C*) and two other randomly selected animals. No effects suggesting vascular damage such as erythrocyte extravasation or damage associated with ischemia, such as dark neurons or necrosis, were detected in the sonicated targets or surrounding regions (Fig. 4*C*).

Controlling the Chemotherapeutic Drug Delivery in F98 Rat Glioma Model. To further validate the controller performance, we tested it in a rat glioma model and with a chemotherapeutic agent (Liposomal DOX) in addition to TB. F98 glioma cells were implanted at two bilateral sites in the striatum, and tumor growth was monitored with MRI (Fig. 5*B*). When the tumors reached ~2 mm in diameter, we sonicated a location centered in one of the tumors and a second (nontumor) location in the same

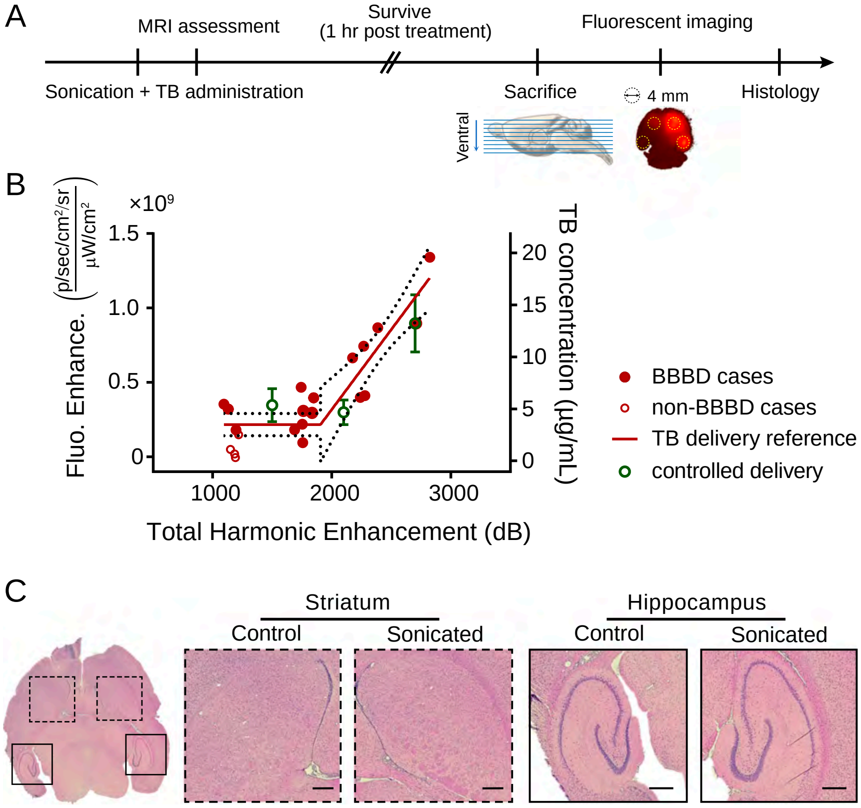

Fig. 4. Controlling model drug delivery across the BBB. (*A*) Schematic illustration of the experimental protocol. (*B*) The correlation between fluorescent intensity enhancement (Fluo. Enhance.) and the total HE. Data in red were acquired from sonications in the striatum and hippocampus with different sonication durations (60, 90, or 120 s; $n = 7$ for each duration). The calibrated delivery reference curve was then constructed by fitting a piecewise linear regression (dotted lines, 95% confidence intervals). Solid red dots represent cases whose fluorescent intensities were more than two SDs above the mean of those in the nonsonicated control group ($n = 10$ for each target); otherwise, data are shown as hollow red dots. Data marked in green show TB delivery in experiments where sonication was performed until total HE reached a preset goal: 1,500 dB ($n = 4$), 2,100 dB ($n = 8$), or 2,700 dB ($n = 5$). Error bars represent SEM. (*C*) Representative H&E-stained brain slices showing no vascular/neuronal damage. (Scale bar, 500 μm.)

hemisphere in the hippocampus. Nonsonicated locations in the contralateral hemisphere served as controls. The BBBD and enhanced permeability of the BTB were confirmed using T1-weighted contrast-enhanced MRI (Fig. 5*D*). MRI contrast signal enhancement suggested the enhanced permeability of both the BBB and the BTB (Fig. 5*E*).

The animals were killed 24 h after sonication to allow time for DOX, which is naturally fluorescent, to be released from the liposomes, and fluorescent imaging was performed (Fig. 5*C*). Consistent with the MRI assessment, both TB (Fig. 5*F*) and DOX (Fig. 5*I*) fluorescent intensities were significantly higher than the controls in both the sonicated tumor and the hippocampus targets. Please note that the level of TB fluorescence was lower here than the results in Fig. 4 would predict. This result is expected because we used a lower TB dose and we waited a longer period between TB administration and sacrifice.

In the tumors, a clear threshold of enhanced delivery was observed for both agents, and a strong correlation between fluorescence and HE_{total} was observed, with $R^2 = 0.86$ and 0.89 for TB and released DOX, respectively (Fig. 5 *G* and *J*). In the hippocampus target, HE_{total} was well-correlated with TB fluorescence ($R^2 = 0.74$; Fig. 5*H*) but less so with DOX ($R^2 = 0.33$; Fig. 5*K*). The variability in the DOX measurements in the hippocampus could have been due to noisy data induced by autofluorescence. DOX fluorescence (excitation/emission: 480/575 nm[38]) overlapped with the yellow/green autofluorescence of tissue. A two-wavelength excitation approach (see *SI Methods* for details) was thus applied in DOX imaging to remove the autofluorescence. Although this approach substantially improved our ability to distinguish DOX fluorescence from autofluorescence, it also reduced the SNR. The relatively weaker fluorescent intensity enhancements in Fig. 5*K* therefore varied more and became more noise prone. Correlation of DOX and TB fluorescence was observed in the tumor but not in the hippocampus (Fig. S3), presumably reflecting this variability observed in DOX fluorescence.

To estimate the dose of the agents delivered to the brain, we calibrated the fluorescent images using standards (filter paper) saturated with serially diluted levels of DOX hydrochloride (unencapsulated DOX) or TB. For both agents, the fluorescence signal increased exponentially as the concentration increased until the signals quenched. DOX fluorescence quenched at 1.28–1.6 mg/mL (64–80% of full strength), and TB fluorescence quenched at around 0.1 mg/mL (Figs. S1 and S2). Over the range of fluorescent intensities detected here and in previous studies, linear relationships for both drugs were observed and used to estimate the delivered doses in Figs. 4 and 5. The estimated DOX concentrations reached up to ∼10 μg/mL, which exceeded levels previously shown to induce tumor regression and improve survival in rat glioma (36), demonstrating the ability of the proposed system to maintain drug dosage within therapeutic thresholds in rat glioma models.

Red blood cell extravasations were found in both the sonicated and the control tumors (Fig. 6*C*). No evident vascular/neuronal damage was found in cases without detected BE (Fig. 6*C*) and in cases where a relatively low level of BE was observed (Fig. 6*A*, in blue; Fig. 6*D*). Our controller minimized inertial cavitation

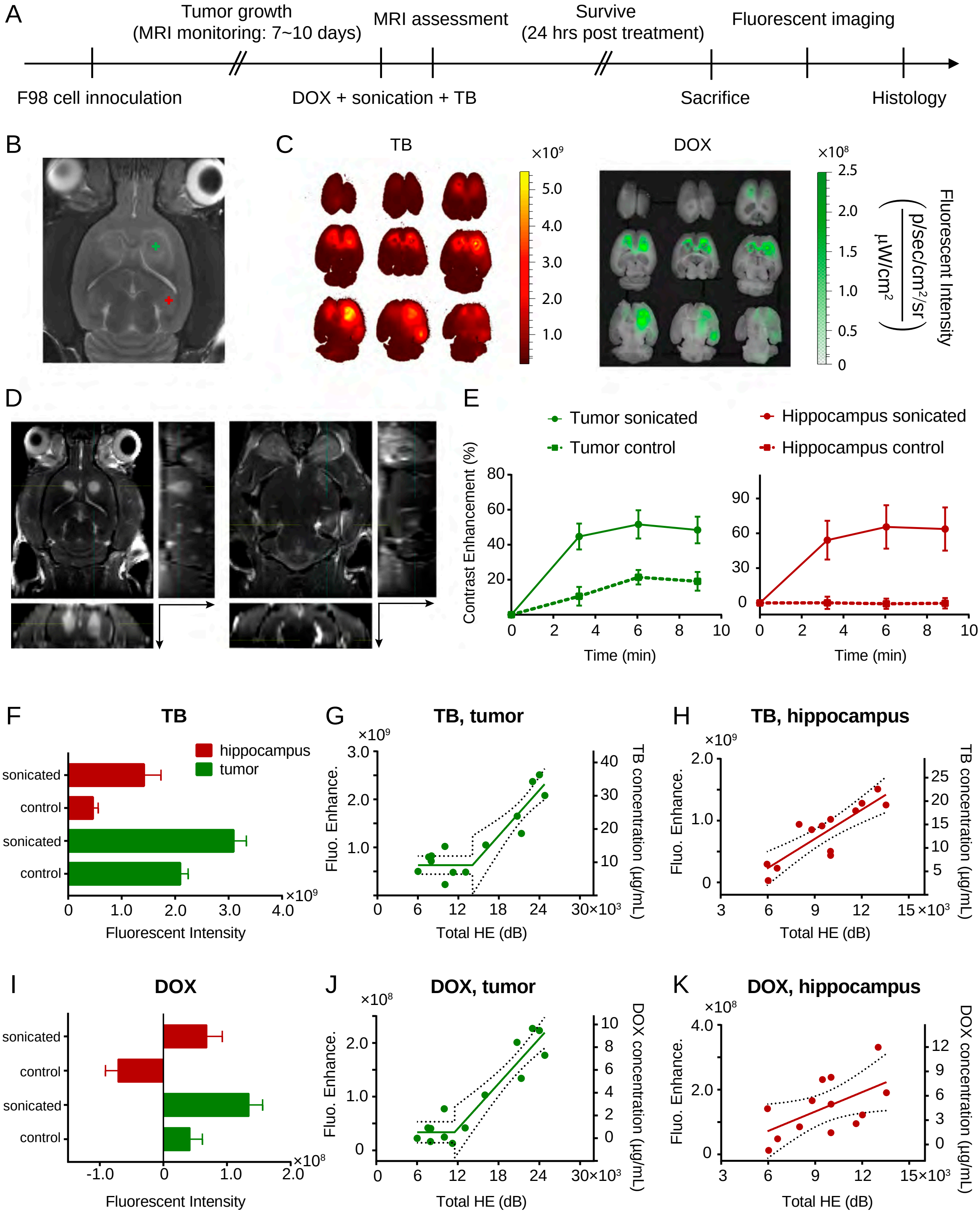

Fig. 5. Controlling chemotherapeutic drug delivery in F98 rat glioma model. (*A*) Schematic illustration of the experimental protocol. (*B*) For treatment planning, an axial representative T2-weighted MR image was acquired on the sonication day for visualizing the anatomical structures and locations of the bilateral tumors. Plus refers to the targeted location. (*C*) Representative fluorescent imaging for TB (*Left*) and DOX (*Right*). (*D*) Contrast-enhanced T1-weighted MR images acquired posttreatment for assessing BTBD/BBBD on the tumor (*Left*) and hippocampus (*Right*) targets. The axial images were reformatted to show sagittal (*Right*) and coronal (*Bottom*) planes. The arrows indicate the direction toward the ventral surface. All MRI and fluorescent images shown in Fig. 5 were obtained from the same animal. (*E*) MRI contrast enhancement (in percent, compared with the baseline images acquired before contrast agent administration) evaluations at three time points post–contrast agent injection. Fluorescent intensities of TB (*F*) and DOX (*I*) in control and sonicated locations were compared. Error bars represent SDs. The relationships between the delivered TB concentration (right axis)/fluorescent enhancement (left axis) and total HE for (*G*) tumor and (*H*) hippocampus targets were assessed (solid lines, piecewise linear regression; dotted lines, 95% confidence intervals). The relationships between delivered DOX concentrations (right axes)/fluorescent enhancement (left axes) and total HE for (*J*) tumor and (*K*) hippocampus targets were also evaluated.

activities by decreasing the pressure amplitude once any BE was detected above the preset threshold. In most cases, BE remained below this threshold, or it only barely exceeded it and was suppressed thereafter (Fig. 6*A*). However, in one case, BE was dramatically higher (orange arrow in Fig. 6*A*). In this extreme example, we detected extravasated erythrocytes in an off-target area (Fig. 6*E*), indicative of sonication-induced vascular damage. T2*- and T2-weighted images showed hypointense and hyperintense regions, respectively, in this area (Fig. 6*F*). Example spectra for the sonication that produced this damage are shown in Fig. 6*B* for cases with and without BE. When strong BE occurred, clear activity was observed around 650 kHz, the sensitive range of the PCD. Without BE, only enhanced HE was observed.

Discussion

The results presented here demonstrate a promising paradigm of treatment control during cavitation-facilitated FUS therapy. To maximize BBBD while avoiding vascular damage, our approach concentrated on sustaining stable cavitation at a predetermined level while suppressing inertial cavitation. In both normal and tumor-bearing rats, we demonstrated that this approach can be used to ensure this result. In our previous work without exposure level control, we observed occasional vascular/tissue damage (11, 36). With control, we were able to deliver a higher DOX dose while maintaining a safe exposure level. This result confirmed the ability of the proposed closed-loop system to tailor the drug delivery dosage within a therapeutically effective range, while improving safety control. Approaches such as this have direct clinical relevance because human trials for BBBD have begun (19, 20).

To maximize this clinical relevance, we chose a low frequency (<500 kHz) of transmission that can circumvent the skull with minimal beam distortion and attenuation. Preclinical investigation in this frequency range is important because the acoustic behavior of microbubbles and corresponding bioeffects may vary as a function of FUS frequency (23, 37). However, such a low frequency is not typically adopted in rodent experiments due to the elongated focal area that exceeds the thickness of a rat brain, leading to internal reflections and standing waves (38). We therefore combined two spherically curved transducers to double the effective aperture size and provide significantly improved focusing in the axial direction. In addition, we used a slightly different frequency offset to modulate the inference pattern from the two FUS sources temporally, which helped to distribute the acoustic energy more evenly and produce homogenous treatment profiles. This design (35) resulted in the BBBD that was fully restricted in the rat brain, providing confidence that the acoustic emissions which were the basis for the feedback control were not contaminated by microbubble activity in extracranial regions.

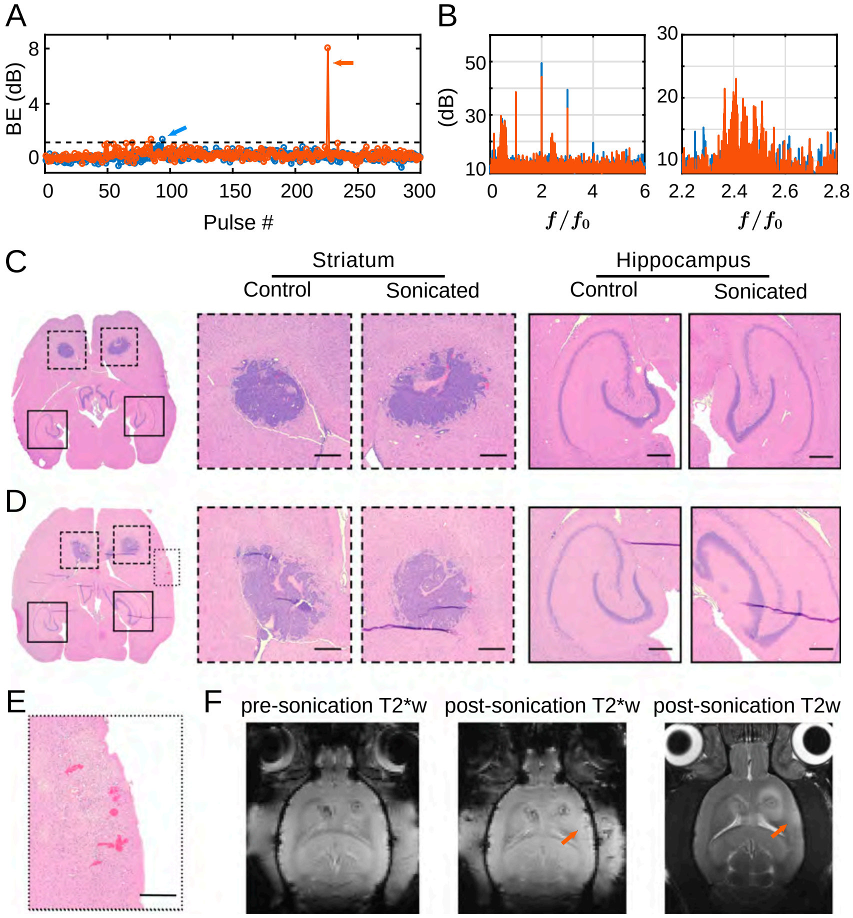

Fig. 6. Safety assessments. (*A*) Two representative examples of BE profiles. The dashed line represents the threshold set in the controller algorithm, above which we considered BE to have occurred. (*B*) Microbubble emission spectra for the bursts indicated by arrows in *A*. Representative H&E evaluations of brain slices when (*C*) BE was not detected and (*D*) a low level of BE was observed. (*E*) H&E stained section showing erythrocytes in an off-target area for a case when large BE was observed (cavitation emissions shown in orange in *A* and *B*). (Scale bar, 500 μm.) (*F*) T2*- and T2-weighted MR images showed hypointense and hyperintense regions, respectively, in the area where we detected red blood cell extravasations.

In the present work, we used the harmonic components of microbubble emissions for the feedback to control the stable cavitation. This approach was based on earlier studies that found a correlation between harmonic activity and BBBD (24). We found that the increase in harmonic activity in dB relative to measurements made without microbubbles (26) was highly linear in the range of stable cavitation and served as a robust signal to control the exposure level in real time. In the rat model used here, the results were repeatable, and a good correlation was found between HE_{total} and the delivered TB and DOX. The repeatability reflects, in part, the simple models used here, where we always targeted the same locations in the brain. Looking forward, to use this clinically we would need to estimate other factors that will affect the relative strength of the harmonics, mainly the attenuation of the received locations due to the skull and the microbubble concentration at the target. These main factors can be estimated beforehand, using CT scans and simulation to estimate the acoustic attenuation (39) and MRI or other imaging methods to estimate the vascular density. It may also be possible to use the onset of subharmonic or ultraharmonic emissions observed when the exposure level is increased as a means to estimate (27, 30). This onset may represent a distinct threshold that depends predominately on the microbubble properties. If that is the case (and not simply a reflection of the noise floor of the detector), one could use the subharmonic to calibrate the sonication and then use the harmonics to modulate the exposure level to produce BBBD at a desired level.

The strengths of the subharmonics or ultraharmonics can also be used as measures of stable cavitation behavior and have been previously reported to be associated with BBBD outcomes (27, 30). Microbubbles in acoustic field typically experience linear to relatively stronger nonlinear oscillation before breaking up. Subharmonics and ultraharmonics are regarded as the acoustic signatures of nonlinear microbubble oscillation (23); however, using these signals poses real challenges in practice. Indeed, there is no evidence that nonlinear oscillations dominate BBBD. Moreover, the detection thresholds of subharmonic/ultraharmonic and broadband components can occur simultaneously over limited acoustic pressure levels (26, 40), making it challenging to find the treatment window free of broadband signals. Finally, subharmonic/ultraharmonic components are relatively weak in power (orders of magnitude less than the harmonics), and their robust detection is more easily compromised by factors that introduce acoustic attenuation and aberration, such as the skull or other intracranial morphologies.

We evaluated two agents, TB and liposomal DOX, which have different sizes, circulation times, and other properties that affect their delivery after BBBD. A good correlation was observed between HE_{total} and TB delivery in both the tumor and the normal brain, consistent with earlier studies in the brain that investigated delivery of an MRI contrast agent (21, 24, 26, 30). A good correlation was also observed with DOX in the tumor but not in the hippocampus. We suspect that the TB measurements were less influenced by autofluorescence and were more robust. Future work using different methods to map DOX concentrations would be necessary to confirm this suspicion. We also observed a correlation between the DOX and TB concentrations in the tumors (Fig. S3). This finding is promising because it suggests that one could use a smaller tracer, such as an MRI contrast agent, to predict the delivery of a much larger liposomal agent. However, this may be challenging because the permeability of the BTB and other factors can change over time and could confound this approach (41).

We controlled inertial cavitation conservatively for BBBD. BE was detected in all animals with histological damage. Other cases with BE detection did not show petechiae in histology, suggesting the threshold we defined as BE may be lower than the level necessary to cause histological damage, and it suggests that we had good PCD sensitivity. However, it is possible that the petechiae occurred outside of the histological sections we investigated. In addition, the strength and the probability of BE detection may act differently in characterizing potential damage. Generally, strong inertial cavitation, even if it occurred rarely, could increase the likelihood of damage. Similar to the probability of inertial cavitation occurrence, the strength of BE is also hard to predict in vivo because microbubbles may collapse individually or as a cluster. This can be affected by FUS parameters, microbubble shell and gas core properties, and physiological changes (ambient pressure, blood flow rate, etc.). Inertial cavitation in large blood vessels and its relationship to vessel damage and BE may also be different from cavitation in capillaries. However, as we have shown in this work, our cavitation controller can decrease the acoustic input and effectively minimize the likelihood of damage. More conservatively, the controller could halt the sonication in the case of BE to evaluate the situation before continuing. The use of automated versus operator-augmented control should be considered carefully when designing the cavitation controller for clinical trials.

Several factors could improve this controller. First, we examined HE and BE for each burst in its entirety before applying the next. A faster controller could be developed to monitor cavitation activity during each burst, which could reduce the time needed to modulate the exposure to the desired level and mitigate vascular damage that might occur in the case of inertial cavitation. Moreover, we only recorded with a single channel, and data from all emission signals in the active field of receiver were used by the controller. However, passive cavitation imaging (PCI) has been recently realized for brain applications (42, 43). Combining PCI into our control system may offer vital spatial information of cavitation activities and prevent cavitation from happening in undesired regions (for example, the damage area shown in Fig. 6*B*). With PCI-fused control, we might be able to identify weak cavitation activities at undesired places early in the sonication and halt or adjust the sonication to avoid damage. Further, our microbubble infusion rate was perhaps not optimal. The power level did not achieve a steady state, suggesting that the microbubble concentration was decreasing. Future work could integrate the infusion pump into the control algorithm to modulate the microbubble concentration along with the FUS exposure level.

It would also be beneficial for future work to expand the histological analyses. Here vascular damage, as evidenced by the presence of petechiae, was observed in one case. With such damage, cell death in nearby areas can occur if the damage is sufficient to cease blood flow. Although other sonicated regions appeared normal, the damage assessments here were limited to histological evaluations at 1 h or 24 h after sonication. Previous work (21) demonstrated that the edema assessed using T2-weighted MRI can peak 24 h after sonication, suggesting that it might be important to evaluate histological effects at later times. It would also be interesting to examine the relationship between acoustic emission and other bioeffects that have been observed in addition to BBBD, vascular damage and edema (44–46).

Some future work is also needed for clinical translation of this control approach. The human skull will attenuate the emission signals, and the detectors will be located farther away from the focal region. Using multiple detectors or improved detector sensitivity may be necessary to compensate for the resulting lower SNR. The clinical systems also have different geometries, and the location of the focal region and the detectors may vary if a phased array transducer is used to steer the beam. These factors will need to be taken into account.

Future studies could also adjust the controlling metrics to accommodate other cavitation-mediated therapies. For ablation and inertial cavitation-enhanced drug delivery, BE can be modulated and/or sustained in a similar fashion as the HE was here. Combined with the clinically available temperature control based on MR thermometry, we envision the reliable treatment control of cavitation to expedite the clinical translation of FUS therapies, especially into drug delivery and brain applications.

In summary, a cavitation emission-based controlling paradigm to modulate the BBBD has been developed. This system is based on the feedback from stable microbubble cavitation, while suppressing the likelihood of damage by avoiding inertial cavitation components. By optimizing acoustic parameters of FUS and the microbubble administration method, we demonstrated the successful controlled chemotherapeutic drug delivery in F98 glioma model in vivo. This validation provides an acoustic means of modulating drug delivery across the BBB/BTB and safety control in real time. These results were obtained using a clinically relevant FUS frequency and are thus expected to be readily translated to human trials for FUS-mediated BBBD. This controller can also potentially be applied to other cavitation-facilitated ultrasound therapies.

Methods

All animal experiments were approved by Harvard Medical School Institutional Animal Care and Use Committees. See *SI Methods* for detailed information including in vivo experiment protocols, cell culture, FUS transmission, detection and control systems, fluorescent imaging, MRI, histology, and data analysis.

ACKNOWLEDGMENTS. We thank Dr. Rolf F. Barth for providing the F98 cells and Dr. Paul Barbone and Dr. Brian Tracey for critical discussion of the results. We also acknowledge Mr. Chao Qi for the help of schematic illustration. This work was supported by National Institutes of Health P01 CA174645.

1. Elias WJ, et al. (2013) A pilot study of focused ultrasound thalamotomy for essential tremor. *N Engl J Med* 369:640–648.
2. McDannold N, et al. (2006) Uterine leiomyomas: MR imaging-based thermometry and thermal dosimetry during focused ultrasound thermal ablation. *Radiology* 240:263–272.
3. Wong AW, et al. (2016) Ultrasound ablation enhances drug accumulation and survival in mammary carcinoma models. *J Clin Invest* 126:99–111.
4. Leslie T, et al. (2012) High-intensity focused ultrasound treatment of liver tumours: Post-treatment MRI correlates well with intra-operative estimates of treatment volume. *Br J Radiol* 85:1363–1370.
5. Hynynen K, McDannold N, Vykhodtseva N, Jolesz FA (2001) Noninvasive MR imaging-guided focal opening of the blood-brain barrier in rabbits. *Radiology* 220:640–646.
6. Burgess A, Hynynen K (2013) Noninvasive and targeted drug delivery to the brain using focused ultrasound. *ACS Chem Neurosci* 4:519–526.
7. Aryal M, Arvanitis CD, Alexander PM, McDannold N (2014) Ultrasound-mediated blood-brain barrier disruption for targeted drug delivery in the central nervous system. *Adv Drug Deliv Rev* 72:94–109.
8. Fan Z, Liu H, Mayer M, Deng CX (2012) Spatiotemporally controlled single cell sonoporation. *Proc Natl Acad Sci USA* 109:16486–16491.
9. Lu Y, et al. (2016) Microbubble-mediated sonothrombolysis improves outcome after thrombotic microembolism-induced acute ischemic stroke. *Stroke* 47:1344–1353.
10. McDannold NJ, Vykhodtseva NI, Hynynen K (2006) Microbubble contrast agent with focused ultrasound to create brain lesions at low power levels: MR imaging and histologic study in rabbits. *Radiology* 241:95–106.
11. Aryal M, Vykhodtseva N, Zhang Y-Z, Park J, McDannold N (2013) Multiple treatments with liposomal doxorubicin and ultrasound-induced disruption of blood-tumor and blood-brain barriers improve outcomes in a rat glioma model. *J Control Release* 169:103–111.
12. Burgess A, et al. (2014) Alzheimer disease in a mouse model: MR imaging-guided focused ultrasound targeted to the hippocampus opens the blood-brain barrier and improves pathologic abnormalities and behavior. *Radiology* 273:736–745.
13. Wang S, Olumolade OO, Sun T, Samiotaki G, Konofagou EE (2015) Noninvasive, neuron-specific gene therapy can be facilitated by focused ultrasound and recombinant adeno-associated virus. *Gene Ther* 22:104–110.
14. Lin C-Y, et al. (2016) Non-invasive, neuron-specific gene therapy by focused ultrasound-induced blood-brain barrier opening in Parkinson's disease mouse model. *J Control Release* 235:72–81.
15. Mead BP, et al. (2016) Targeted gene transfer to the brain via the delivery of brain-penetrating DNA nanoparticles with focused ultrasound. *J Control Release* 223:109–117.
16. McDannold N, Zhang Y, Vykhodtseva N (2017) The effects of oxygen on ultrasound-induced blood-brain barrier disruption in mice. *Ultrasound Med Biol* 43:469–475.
17. McDannold N, Arvanitis CD, Vykhodtseva N, Livingstone MS (2012) Temporary disruption of the blood-brain barrier by use of ultrasound and microbubbles: Safety and efficacy evaluation in rhesus macaques. *Cancer Res* 72:3652–3663.
18. Marquet F, Tung Y-S, Teichert T, Ferrera VP, Konofagou EE (2011) Noninvasive, transient and selective blood-brain barrier opening in non-human primates in vivo. *PLoS One* 6:e22598.
19. Carpentier A, et al. (2016) Clinical trial of blood-brain barrier disruption by pulsed ultrasound. *Sci Transl Med* 8:343re2.
20. Huang Y, et al. (2016) Initial experience in a pilot study of blood-brain barrier opening for chemo-drug delivery to brain tumors by MR-guided focused ultrasound. *Proceedings of the International Society for Magnetic Resonance in Medicine* (International Society for Magnetic Resonance in Medicine, Berkeley, CA), abstr 450.
21. Sun T, et al. (2015) Acoustic cavitation-based monitoring of the reversibility and permeability of ultrasound-induced blood-brain barrier opening. *Phys Med Biol* 60:9079–9094.
22. Neppiras EA (1984) Acoustic cavitation series: Part one: Acoustic cavitation: An introduction. *Ultrasonics* 22:25–28.
23. Bader KB, Holland CK (2013) Gauging the likelihood of stable cavitation from ultrasound contrast agents. *Phys Med Biol* 58:127–144.
24. McDannold N, Vykhodtseva N, Hynynen K (2006) Targeted disruption of the blood-brain barrier with focused ultrasound: Association with cavitation activity. *Phys Med Biol* 51:793–807.
25. Tung Y-S, Choi JJ, Baseri B, Konofagou EE (2010) Identifying the inertial cavitation threshold and skull effects in a vessel phantom using focused ultrasound and microbubbles. *Ultrasound Med Biol* 36:840–852.
26. Arvanitis CD, Livingstone MS, Vykhodtseva N, McDannold N (2012) Controlled ultrasound-induced blood-brain barrier disruption using passive acoustic emissions monitoring. *PLoS One* 7:e45783.
27. Tsai C-H, Zhang J-W, Liao Y-Y, Liu H-L (2016) Real-time monitoring of focused ultrasound blood-brain barrier opening via subharmonic acoustic emission detection: Implementation of confocal dual-frequency piezoelectric transducers. *Phys Med Biol* 61:2926–2946.
28. Chen W-S, Brayman AA, Matula TJ, Crum LA (2003) Inertial cavitation dose and hemolysis produced in vitro with or without Optison. *Ultrasound Med Biol* 29:725–737.
29. Qiu Y, et al. (2010) The correlation between acoustic cavitation and sonoporation involved in ultrasound-mediated DNA transfection with polyethylenimine (PEI) in vitro. *J Control Release* 145:40–48.
30. O'Reilly MA, Hynynen K (2012) Blood-brain barrier: Real-time feedback-controlled focused ultrasound disruption by using an acoustic emissions-based controller. *Radiology* 263:96–106.
31. Sun T, Jia N, Zhang D, Xu D (2012) Ambient pressure dependence of the ultra-harmonic response from contrast microbubbles. *J Acoust Soc Am* 131:4358–4364.
32. Dayton PA, et al. (1997) A preliminary evaluation of the effects of primary and secondary radiation forces on acoustic contrast agents. *IEEE Trans Ultrason Ferroelectr Freq Control* 44:1264–1277.
33. Chen X, Wang J, Pacella JJ, Villanueva FS (2016) Dynamic behavior of microbubbles during long ultrasound tone-burst excitation: Mechanistic insights into ultrasound-microbubble mediated therapeutics using high-speed imaging and cavitation detection. *Ultrasound Med Biol* 42:528–538.
34. Chen X, et al. (2011) An alternating focused ultrasound system for thermal therapy studies in small animals. *Med Phys* 38:1877–1887.
35. Sun T, et al. (2017) Transcranial cavitation-mediated ultrasound therapy at sub-MHz frequency via temporal interference modulation. *Appl Phys Lett* 111:163701.
36. Aryal M, Vykhodtseva N, Zhang Y-Z, McDannold N (2015) Multiple sessions of liposomal doxorubicin delivery via focused ultrasound mediated blood-brain barrier disruption: A safety study. *J Control Release* 204:60–69.
37. McDannold N, Vykhodtseva N, Hynynen K (2008) Blood-brain barrier disruption induced by focused ultrasound and circulating preformed microbubbles appears to be characterized by the mechanical index. *Ultrasound Med Biol* 34:834–840.
38. O'Reilly MA, Huang Y, Hynynen K (2010) The impact of standing wave effects on transcranial focused ultrasound disruption of the blood-brain barrier in a rat model. *Phys Med Biol* 55:5251–5267.
39. Yin X, Hynynen K (2005) A numerical study of transcranial focused ultrasound beam propagation at low frequency. *Phys Med Biol* 50:1821–1836.
40. Gruber MJ, Bader KB, Holland CK (2014) Cavitation thresholds of contrast agents in an *in vitro* human clot model exposed to 120-kHz ultrasound. *J Acoust Soc Am* 135:646–653.
41. Aryal M, Park J, Vykhodtseva N, Zhang Y-Z, McDannold N (2015) Enhancement in blood-tumor barrier permeability and delivery of liposomal doxorubicin using focused ultrasound and microbubbles: Evaluation during tumor progression in a rat glioma model. *Phys Med Biol* 60:2511–2527.
42. Arvanitis CD, Livingstone MS, McDannold N (2013) Combined ultrasound and MR imaging to guide focused ultrasound therapies in the brain. *Phys Med Biol* 58:4749–4761.
43. O'Reilly MA, Jones RM, Hynynen K (2014) Three-dimensional transcranial ultrasound imaging of microbubble clouds using a sparse hemispherical array. *IEEE Trans Biomed Eng* 61:1285–1294.
44. Raymond SB, Skoch J, Hynynen K, Bacskai BJ (2007) Multiphoton imaging of ultrasound/Optison mediated cerebrovascular effects in vivo. *J Cereb Blood Flow Metab* 27:393–403.
45. Kovacs ZI, et al. (2017) Disrupting the blood-brain barrier by focused ultrasound induces sterile inflammation. *Proc Natl Acad Sci USA* 114:E75–E84.
46. McMahon D, Bendayan R, Hynynen K (2017) Acute effects of focused ultrasound-induced increases in blood-brain barrier permeability on rat microvascular transcriptome. *Sci Rep* 7:45657.

47. Barth RF, Kaur B (2009) Rat brain tumor models in experimental neuro-oncology: The C6, 9L, T9, RG2, F98, BT4C, RT-2 and CNS-1 gliomas. *J Neurooncol* 94:299–312.
48. Treat LH, McDannold N, Zhang Y, Vykhodtseva N, Hynynen K (2012) Improved anti-tumor effect of liposomal doxorubicin after targeted blood-brain barrier disruption by MRI-guided focused ultrasound in rat glioma. *Ultrasound Med Biol* 38:1716–1725.
49. O'Reilly MA, Muller A, Hynynen K (2011) Ultrasound insertion loss of rat parietal bone appears to be proportional to animal mass at submegahertz frequencies. *Ultrasound Med Biol* 37:1930–1937.
50. Samuel S, Miller DL, Fowlkes JB (2006) The relationship of acoustic emission and pulse-repetition frequency in the detection of gas body stability and cell death. *Ultrasound Med Biol* 32:439–447.
51. Kaya M, Gregory TS, 5th, Dayton PA (2009) Changes in lipid-encapsulated microbubble population during continuous infusion and methods to maintain consistency. *Ultrasound Med Biol* 35:1748–1755.
52. Bakay L, Ballantine HT, Jr, Hueter TF, Sosa D (1956) Ultrasonically produced changes in the blood-brain barrier. *AMA Arch Neurol Psychiatry* 76:457–467.

Supporting Information

Sun et al. 10.1073/pnas.1713328114

SI Methods

Animals and Tumor Model. A total of 42 male Sprague–Dawley rats and 14 male Fischer CDF (for the F98 tumor model) rats were used (~300 g; Charles River Laboratories, Inc.). Animals were anesthetized by i.p. injections of ketamine (80 mL/kg/h) and xylazine (10 mL/kg/h) for FUS experiments and with 2% isoflurane during MRI. A catheter was placed in the tail vein for i.v. administration, and the hair on the scalp was removed with clippers and depilatory cream for better ultrasound propagation.

For the experiments in the tumor model, wild-type F98 cells [passage number 6, provided by Rolf F. Barth (47) at the Department of Pathology, The Ohio State University, Columbus, OH] were cultured in Dulbecco's modified Eagle medium (1×) supplemented with 10% FBS and 0.1% Penicillin Streptomycin in a humidified incubator with 5% CO_2 at 37 °C. Following the surgical procedure as previously described (48), 4-μL cell suspension (2×10^5 cells) was injected into the caudate putamen bilaterally at 3.5 mm from the dura surface using a 10-μL gastight syringe (Hamilton) in Fischer rats. Animal behavior was monitored daily after surgery and the sutures were removed 5 d later.

Animals were killed either 1 h (healthy rats) or 24 h (tumor-bearing rats) after FUS and TB administration, under deep anesthesia with ketamine/xylazine. The brains were fixed by transcardial perfusion using 0.9% NaCl (100 mL) followed by 10% buffered formalin phosphate (250 mL). The brains were then harvested and soaked in 10% buffered formalin phosphate for at least 24 h before being sectioned into 1-mm transverse blocks for fluorescent imaging.

FUS System. A dual-transducer system for FUS transmission was designed and built in house. The system consists of two air-backed, spherically focused transducers (diameter/radius of curvature: 10/8 cm) with a resonant frequency at 274.3 kHz. The transducers were mounted in an acrylic holder at an angle of 102° with respect to each other (an angle greater than 90° was used to maximize the space between the transducers for the PCD). To break up the interference pattern in the focal region, one of the transducers was operated at a frequency of 31 Hz higher than the other. The burst length was one period of the beat frequency (32.3 ms), and the bursts were applied at a PRF of 1 or 4 Hz. A frequency difference of 31 Hz was selected so that integration of the modulation envelope over one half of a period was close to that of a 10-ms burst applied at a single frequency, a value commonly used for BBBD. The two FUS transducers were driven by two function generators (33220 A; Agilent) and two amplifiers (43 dB gain, LZY-22+; Mini-Circuits). The transducers were matched to 50 ohms, and the electrical power output was measured using a power meter (E4419 B; Agilent) and dual-directional coupler (C5948-10; Werlatone). The transducers were calibrated using scans of the focal plane acquired with a needle hydrophone (HNC-1000; Onda) and radiation force balance measurements to estimate the peak intensity at the focus. The pressure amplitude at the focus was estimated from the intensity assuming linear propagation. The pressure amplitude at the combined focus of the two transducers was estimated from the needle hydrophone after calibrating it by driving one transducer and placing a needle hydrophone at its focus. Pressure amplitudes presented here are those estimated in water considering the skull insertion loss (49).

Acoustic Emission Recording and Control. An elliptical air-backed passive cavitation detector with dimensions of 5 × 3 cm and a center frequency of 650 kHz (bandwidth: 75%) was used to record the acoustic emissions during the sonications. A digital filter (model 3944; Krohn–Hite) operating as Butterworth notch filter (stop band: 150–466 kHz) was used to suppress the fundamental frequency component in the recorded emission signals before the analysis for controller. It also amplified the signal by 20 dB. Emission signals were recorded with a high-speed digitizer (PXIe 1073; National Instruments) at a sampling rate of 5 MHz. Power spectra [$PSD(f)$] were then converted using fast Fourier transform and a Hanning window. The cavitation enhancement was calculated as the relative signal strength in dB for each burst:

$$S = \frac{10}{W}\log_{10}\left(\int_{W}\frac{PSD(f)}{PSD_{BL}(f)}df\right),$$

where $PSD_{BL}(f)$ is the power spectra obtained without microbubbles and W is the bandwidth (harmonic components, 300 Hz; broadband emission, 40 kHz) (26, 50). All time and frequency analysis, feedback controlling operations, and spectrum/controller profile display were performed in real time using in-house developed MATLAB scripts. The bursts were applied before verifying that the last one was at a safe level. If BE was detected in the closed-loop controlling, the electric input from the function generators would decrease by 1 mV.

Microbubble Administration. The microbubble contrast agent Optison (GE Healthcare) was injected either as a 4.1-s bolus or as the same bolus followed by a constant infusion. The infusion rate was 0.08 mL/min. The injections were performed with a computer-controlled syringe pump (NE-1000; New Era Pump Systems Inc.). A mechanical system was constructed that constantly rotated the syringe to keep the microbubbles mixed throughout the experiments. The syringe was rotated ±360° at a rate of ~15 rotations per minute (51).

Fluorescent Dye and Chemotherapeutic Drug. 0.08 g TB powder (MP Biomedicals) was dissolved in 2.5 mL of 0.45% NaCl and heated until boiling. This solution was then passed through a filter (MILX GV 0.22UM PVDF; Millipore Cor.) and then slowly injected i.v. at a dose of 0.1 g TB per kg of body weight (52) to visualize the BBB disruption after euthanasia. In the experiments with tumor-bearing rats, liposomal DOX chemotherapy (Doxoves, Liposomal Doxorubicin HCL, 2.0 mg/mL; FormuMax Scientific, Inc.) was administrated i.v. at a dose of 2 mg/kg before sonication following a protocol we developed previously (11). To avoid fluid overload, only a half-dose of TB was administered in these animals.

MRI. All MRI assessments were performed in a 7T Bruker Biospec animal MR-system (Biospec; Bruker). A high-resolution T2-weighted (T2w) sequence was used to access tumor volume until the tumor diameter was about 2 mm. After sonication, T1-weighted (T1w), T2w, and T2*-weighted (T2*w) images were obtained for confirming the BBBD and potential damage. T2*w and T2w images were first obtained to detect potential hemorrhage and edema that may have occurred during the sonications. Contrast-enhanced T1w imaging was then used to access BBB/BTB permeability. T1w scans were acquired before and repeated three times after a bolus injection of 0.25 mL/kg gadopentetate dimeglumine (Gd-DTPA, molecular weight 938 Da, Magnevist; Bayer HealthCare Pharmaceuticals Inc.). All MRI parameters are shown in Table S1.

Fluorescent Imaging. Fluorescent images were acquired by the IVIS Lumina Series III imaging system (Perkin-Elmer). Data acquisition and quantification were performed in Living Image software (V4.3; Perkin–Elmer). To image TB, we used 1-s exposure time and a 640-nm/Cy 5.5 (excitation/emission) filter set. Exposure time was increased to 5 s, and the filter set was changed to 530 nm/DsRed when imaging DOX. For DOX fluorescence, the image was subtracted by 50% the intensity of an additional image that was obtained with a 470 nm/DsRed filter to reduce contributions from autofluorescence. Because DOX fluorescence is quenched when encapsulated, we assumed that our measurements were of free drug released from the liposomes over 24 h after delivery across the BBB/BTB.

Histology. Histological assessment of the sonication effects was obtained in representative examples. Following fluorescent assessments, tissue blocks were embedded in paraffin and sectioned into 5-μm serial transverse sections (perpendicular to the direction of ultrasound propagation). Every 20th section (100 μm apart) was stained with hematoxylin and eosin (H&E) for histological evaluations.

Data Analysis. Fluorescent intensities in regions of interest (ROI; circles with 4 mm in diameter) were quantified as radiant efficiency [fluorescence emission radiance per incident excitation irradiance: $(\text{photons/s/cm}^2/\text{steradian})/(\mu\text{W/cm}^2)$]. We compared fluorescent intensity in the sonicated region to similar locations in control animals that did not receive FUS. If the intensity was less than the mean value plus two SDs in the control ROI, the BBB was considered to not be disrupted. Fluorescent enhancement was quantified as the fluorescent intensity of treated location subtracted by the mean intensity of the control location without sonication. The contrast signal in MRI before and after Gd-DTPA administration was evaluated in a 3 × 3 voxel ROI. Contrast enhancement was calculated as the percentage enhancement relative to the contrast intensity in the same ROI before Gd-DTPA injection. Statistical comparisons between data pairs were performed using ordinary two-way ANOVA with a Tukey multicomparison test in GraphPad (PRISM 6.0). The threshold for statistical significance was $P < 0.05$. Linear regressions or segmental linear regressions were analyzed in MATLAB or GraphPad.

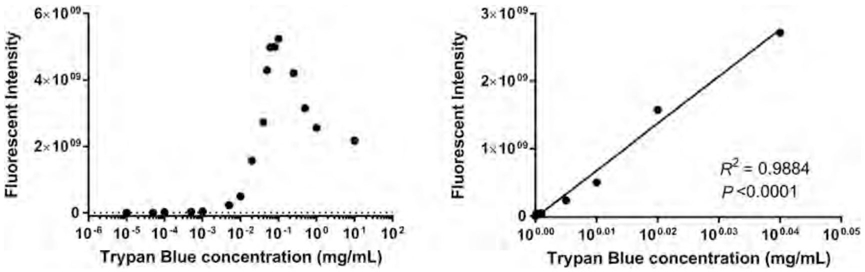

Fig. S1. Fluorescent intensities of calibration standards with different TB concentrations. TB fluorescence was found to quench at around 0.1 mg/mL The zoomed-in plot (*Right*) showed a linear relationship over the range of fluorescent intensities detected in Figs. 4 and 5. This relationship was used to estimate the delivered TB doses.

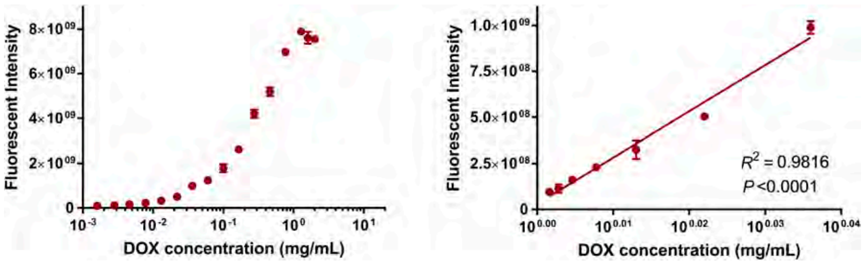

Fig. S2. Fluorescent intensities of calibration standards with different DOX concentrations. Quenching effect was observed as well: DOX fluorescence quenched at 1.28–1.6 mg/mL. The zoomed-in plot (*Right*) showed a linear relationship over the range of fluorescent intensities detected in Figs. 4 and 5. This relationship was used to estimate the delivered DOX doses.

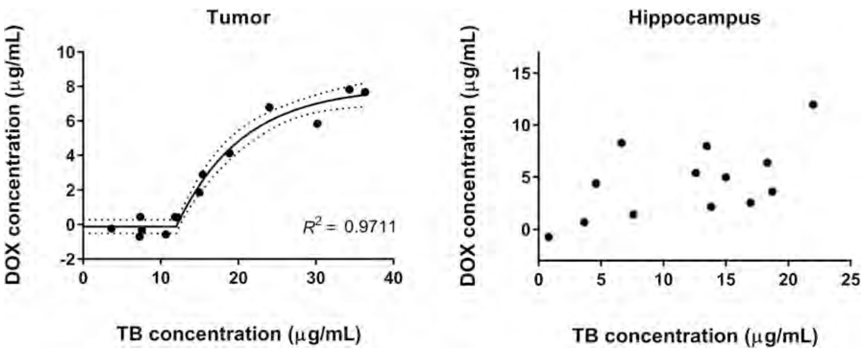

Fig. S3. TB–DOX delivery relationship in tumor and hippocampus targets. TB and DOX delivery doses were compared in tumor-bearing striatum targets (*Left*) and non–tumor-bearing hippocampus targets (*Right*).

Table S1. MRI parameters

Parameter	T2-w imaging	T1-w imaging	T2*-w imaging
Sequence	RARE-ETL: 14	RARE − ETL: 4	Gradient echo − $\alpha = 30$
Echo time, ms	52	18	15
Repetition time, ms	3,500	602	495
Field of view, mm	30 × 25.6	35 × 35	35 × 35
Matrix	300 × 252	128 × 128	128 × 128
No. of averages	6	4	2
Slice thickness, mm	1	1	1